energy&fuels

pubs.acs.org/EF

Article

Preadsorbed SO_3 Inhibits Oxygen Atom Activity for Mercury Adsorption on Cu/Mn Doped $CeO_2(110)$ Surface

Tao Wang,* Yihuan Yang, Jiawei Wang, Baharak Sajjadi, Wei-Yin Chen, Yongsheng Zhang,* and Wei-Ping Pan

Cite This: https://dx.doi.org/10.1021/acs.energyfuels.9b04508

Read Online

ACCESS | Metrics & More | Article Recommendations

ABSTRACT: The coadsorption of Hg^0 and SO_3 on pure and Cu/Mn doped $CeO_2(110)$ surfaces were investigated using the Density Functional Theory (DFT) method. A p (2 × 2) supercell periodic slab model with seven atomic layers was constructed to represent the $CeO_2(110)$ surface. The results indicated that Hg^0 physically adsorbed on the $CeO_2(110)$ surface, while Hg^0 chemically adsorbed on the Cu/Mn doped $CeO_2(110)$ surface, which agree well with the experimental results that Cu and Mn doped CeO_2 greatly improved the Hg^0 adsorption capacity of the adsorbent. The calculated results suggested that SO_3 more easily adsorbs on the above three surfaces than Hg^0 due to the higher adsorption energy. The adsorption configurations and electronic structures indicated SO_3 reacted with O atoms of the surface to form SO_4^{2-} species. Hence, SO_3 inhibits Hg^0 adsorption on the $CeO_2(110)$ surface by competing with Hg^0 for surface lattice oxygen. In addition, SO_3 decreased the activity of the surface O atoms, which directly caused the negative effect on Hg^0 adsorption.

1. INTRODUCTION

Mercury is a heavy metal element with volatility, migration, and bioaccumulation,[1] which has received a great deal of attention in recent years. In coal-fired flue gas, mercury has three basic states, elemental mercury (Hg^0), oxidized mercury (Hg^{2+}), and particulate mercury (Hg^p).[2,3] It is difficult to remove Hg^0 using existing air pollution control devices since the elemental mercury has low solubility and reactivity. Selective catalytic reduction (SCR) catalysts can oxidize Hg^0 to Hg^{2+}, and then Hg^{2+} is captured by wet flue gas desulfurization (WFGD) due to its solubility.[4,5] Therefore, the combined utilization of SCR catalysts and the WFGD system is an effective technology for Hg^0 removal. Metal oxides such as V_5O_2, Fe_2O_3, and Al_2O_3 have been extensively studied due to their high levels of catalytic activity.[6−8] CeO_2 is also an excellent candidate with sulfur resistance, nontoxicity, and low-cost.[9−11] The interchange between Ce^{3+} and Ce^{4+} in CeO_2 plays an important role in its redox properties,[12−14] while the pure CeO_2 exhibited poor catalytic performance due to limited oxygen storage capacity. Previous research has indicated that doping with heteroatoms on CeO_2 can greatly improve its catalytic activity.[15−17] Copper (Cu) and manganese (Mn), as transition metals, react with the CeO_2 matrix to generate Cu−O−Ce or Mn−O−Ce structure, which exhibit high catalytic reactivity.[8,18] Wang et al.[19] found that Mn doping significantly enhanced the surface activity since surface oxygen vacancies were generated on the surface of Mn doped $CeO_2(111)$. Guo et al.[20] found that the energy barrier of CO_2 dissociation on the Cu doped $CeO_2(111)$ surface was only 0.90 eV, which was much lower than that on the perfect $CeO_2(111)$ surface, 3.70 eV. CeO_2 has three stable low index surfaces: $CeO_2(110)$, $CeO_2(111)$, and $CeO_2(100)$.[21,22] Previous studies have shown the performance of Hg^0 adsorbed on metal doped $CeO_2(111)$ surfaces.[23,24] Compared with $CeO_2(111)$, the $CeO_2(110)$ surface presents some unique properties. The $CeO_2(110)$ surface has a higher surface energy and lower oxygen vacancy formation energy than the $CeO_2(111)$ surface.[18] In addition, the $CeO_2(110)$ surface has a unique open plane structure which could provide different adsorption sites for mercury.[25]

The SO_3 concentration is much higher than Hg^0 in the flue gas, hence the presence of SO_3 will have a certain effect on the removal of Hg^0. Many previous experimental studies have shown that SO_3 affects the catalytic oxidation of Hg^0. Yang et al.[26] found that CeO_2 oxidized SO_2 to form SO_3, which subsequently reacted with Hg^0 to produce $HgSO_4$ under simulated flue gas. Zhuang et al.[27] found that SO_3 inhibited the oxidation of mercury; the oxidized mercury in the SCR outlet decreased from 71% to 45% when 50 ppm of SO_3 was added to the flue gas across the SCR. Sjostrom et al.[28] pointed out that mercury capture decreased from 85% to 17% after the addition of 10.7 ppm of SO_3. However, Cao et al.[29] indicated that the Hg^0 oxidation efficiency increased by approximately 20% when adding 50 ppm of SO_3 to flue gas in the SCR slipstream reactor. From a theoretical aspect, He et al.[30] indicated that SO_3 decreased the adsorption energy of Hg^0 on a carbonaceous surface since SO_3 suppressed the activity of its

Received: December 28, 2019
Revised: March 8, 2020
Published: March 10, 2020

next-nearest-neighbor carbon atom. However, few theoretical studies investigated the adsorption mechanism of Hg^0 and SO_3 on the $CeO_2(110)$ surface. DFT calculation has been widely used in the study of Hg^0 adsorption on different metal or metal oxide surfaces.[31] This simulation results can also provide additional information with the experimental results. Thus, combined, the experimental and simulation calculation will be the best way to better understand the mechanism of mercury adsorption.

In this study, the DFT method was conducted to investigate the effect of SO_3 on Hg^0 adsorption on pure and Cu/Mn doped $CeO_2(110)$ surfaces. The adsorption energy, adsorption configuration, and electronic structure were calculated to study the effect of SO_3 and Cu/Mn doping on Hg^0 adsorption. The mercury adsorptions on CeO_2, Cu/CeO_2, and Mn/CeO_2 catalysts were conducted by experimental methods to further study the Hg^0 adsorption performance on different catalysts.

2. COMPUTATIONAL AND EXPERIMENTAL SECTION

2.1. Computational Method. In this study, all the density functional theory calculations were performed using the DMol^3 software.[32] The exchange-correlation potential was calculated by the GGA-PBE method.[33,34] The double numerical basis set, plus polarization with p-functions (DNP), was applied for the molecular orbitals. The core DFT semicore pseudopotential (DSPP) method was used to set the core treatment of Hg, Cu, and Ce, while the all-electron method was applied to O and S. Spin-polarized geometry optimization and a 5.0 Å global orbital cut off was used during the calculations. A 0.005 Ha smearing was applied to increase the computing speed. Three convergence criteria were used for geometric optimization: (1) a maximum force tolerance of 0.002 Ha/Å, (2) a maximum displacement tolerance of 0.005 Å, and (3) a maximum energy tolerance of 1×10^{-5} Ha.

2.2. Computational Models. The crystal configuration of CeO_2 is a face-centered cubic structure with a space group $Fm\bar{3}m$, as shown in Figure 1A. The Monkhorst-pack grid parameters of the unit cell are $4 \times 4 \times 4$. The optimized unit cell parameters ($a = b = c = 5.465$ Å) were within 1.1% error of the experimental lattice constants ($a = b = c = 5.411$ Å).[35]

In comprehensive consideration of calculation accuracy and computing resources, a p (2×2) supercell periodic slab model with seven atomic layers was constructed, as shown in Figure 1B. The lower two atomic layers are fixed, and the upper five atomic layers are fully relaxed. A 15 Å thick vacuum region was set so that the energy effect of interactions between the slabs can be neglected. The Monkhorst-pack grid parameters of the $CeO_2(110)$ surface are $3 \times 3 \times 1$. There are two kinds of adsorption sites: the surface sites (X_{suf}) and the subsurface sites (X_{sub}). The eight adsorption sites, O_{suf}, O_{sub}, Ce_{suf}, Ce_{sub}, $hollow_{sub}$, $hollow_{suf}$, $Ce{-}O_{sub}$, and $Ce{-}O_{suf}$, are shown in Figure 1C. The surface O atoms at the different locations are numbered (O(1) to O(8)) to facilitate following the calculation and analysis, as shown in Figure 1C.

Correcting the f orbital of Ce by Hubbard parameter U can describe the electronic structure of CeO_2 more accurately. However, Kumari et al.[36] stated that the effect of Hubbard parameter U correction on the oxygen vacancy formation energy of the stoichiometric $CeO_2(110)$ surface is slight. Some research shows that using only a DFT method without Hubbard parameter U correction can also provide a reasonable prediction of mercury adsorption on the CeO_2 surfaces.[23,24] Therefore, the calculation method of DFT without Hubbard parameter U correction is selected in this study.

SO_3 is calculated by using the same geometric optimization parameters as CeO_2 in a $10 \times 10 \times 10$ Å cell. The calculated bond lengths of S−O are 1.46 Å and the three bond angles are 119.98°, 119.95°, and 120.07°, respectively. The calculation parameters of SO_3 are in good agreement with the previous computational values.[37]

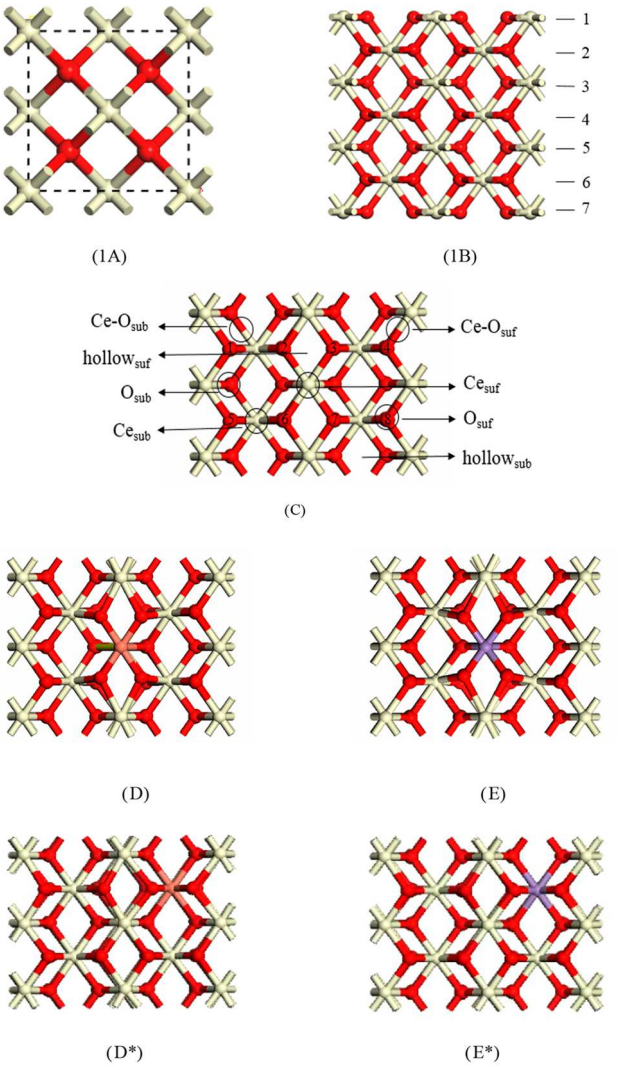

Figure 1. (A) CeO_2 unit cell; (B) side view of $CeO_2(110)$; (C) top view of $CeO_2(110)$; (D) top view of Cu-$CeO_2(110)$; (E) top view of Mn-$CeO_2(110)$; (D*) top view of Cu-$CeO_2(110)$*; (E*) top view of Mn-$CeO_2(110)$*. (The red balls stand for O; the white balls stand for Ce; the pink balls stand for Cu; the purple balls stand for Mn).

There are two kinds of atoms exposed to the environment on the $CeO_2(110)$ surface, which is shown in Figure 1C as Ce_{suf} and Ce_{sub}. To study the effect of metal doping on Hg^0 adsorption, Cu and Mn atoms take the place of the Ce atoms in the first (Ce_{suf}) and second (Ce_{sub}) atomic layers of the $CeO_2(110)$ surface, respectively. Then, the Cu and Mn doped $CeO_2(110)$ surfaces were optimized by the same computational parameters as the $CeO_2(110)$ surface. The optimized Cu and Mn doped $CeO_2(110)$ surfaces are shown in Figure 1D to E. Figure 1D and E show that the Cu and Mn atoms take the place of the Ce atoms in the first atomic layer of the $CeO_2(110)$ surface, respectively, denoted as Cu-$CeO_2(110)$ and Mn-$CeO_2(110)$. Figure 1D* and E* show that the Cu and Mn atoms take the place of the Ce atoms in the second atomic layer of the $CeO_2(110)$ surface, respectively, denoted as Cu-$CeO_2(110)$* and Mn-$CeO_2(110)$*.

2.3. Computational Parameters. The adsorption energy (E_{ads}) is defined as follows:

$$E_{ads} = E_{slab+X} - E_{slab} - E_X \quad (1)$$

https://dx.doi.org/10.1021/acs.energyfuels.9b04508
Energy Fuels XXXX, XXX, XXX−XXX

where E_{slab+X} represents the total energy of the X molecule adsorbed by the substrate model and E_X and E_{slab} are for the total energy of the X molecule and substrate model, respectively. A negative adsorption energy indicates that the absorption process is an exothermic reaction, while a positive value indicates an endothermic reaction. The adsorption energy was calculated at 0 K by default, and the more negative the adsorption energy, the easier the reaction process will occur.

Hirshfeld population was used to determine the charge distribution of atoms in adsorption configurations. It suggests that the number of electrons around the atom is larger than that of the nuclear charges when the Hirshfeld charges are less than zero; hence, the atom becomes electronegative. Conversely, the atom is electropositive when the Hirshfeld charges are greater than zero.

2.4. Experimental Method. In order to verify the simulation results of mercury adsorption on the catalyst surface, CeO_2, Cu/CeO_2, and Mn/CeO_2 catalysts were prepared to study the process of mercury adsorption, as shown in Figure 2. The Cu/CeO_2 and Mn/CeO_2 were prepared using an incipient wetness impregnation method. The CeO_2 powder and $Cu(NO_3)_2{\cdot}3H_2O$ mixture or 50% $Mn(NO_3)_2$ solution was placed in a beaker and dissolved in deionized water. The resulting solutions were then magnetically stirred for 12 h and further dried at 105 °C for 24 h. This was followed by calcination in air at 550 °C for 3 h. Finally, the obtained catalyst was crushed to a size of 40−60 mesh. The designated Cu/Ce and Mn/Ce molar ratios were 5:100, and the obtained catalysts were abbreviated as Cu/CeO_2 and Mn/CeO_2. The experimental setup and Hg^0 adsorption efficiency are described in our previous research.[38] Briefly, 0.4 g of the catalyst was fixed with quartz wool in a quartz tube reactor which was placed in an electric resistance furnace, and the experiment was carried out at 200 °C. The gas flow rate of the experiment was 1 L/min, and the initial concentration of Hg^0 was 20 $\mu g/m^3$. Hg^0 was delivered by N_2 from PSA Cavkit and measured by an online mercury analyzer (RA 915M, Lumex, Russia).

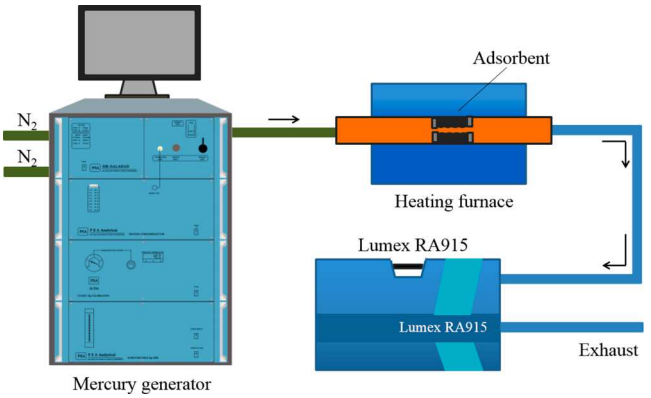

Figure 2. Schematic diagram of Hg^0 adsorption on catalysts.

3. RESULTS AND DISCUSSION

3.1. Hg^0 Adsorption on the CeO_2(110) Surface. The Hg^0 adsorption mechanism on the CeO_2(110) surface was calculated and analyzed. All possible sites that could adsorb Hg^0 were considered. Three stable structures were obtained, which are shown in Figure 3. The corresponding geometry parameters are listed in Table 1. The adsorption energies of the three models are −6.36, −6.95, and −13.82 kJ/mol, respectively, suggesting that the Hg atom has a physical interaction with the CeO_2(110) surface. According to the adsorption energies, the most stable adsorption configuration is model 3C where the Hg^0 adsorbed on the location of $hollow_{sub}$, with the bond lengths of Hg−O(2) and Hg−O(6) being 3.567 and 3.588 Å, respectively.

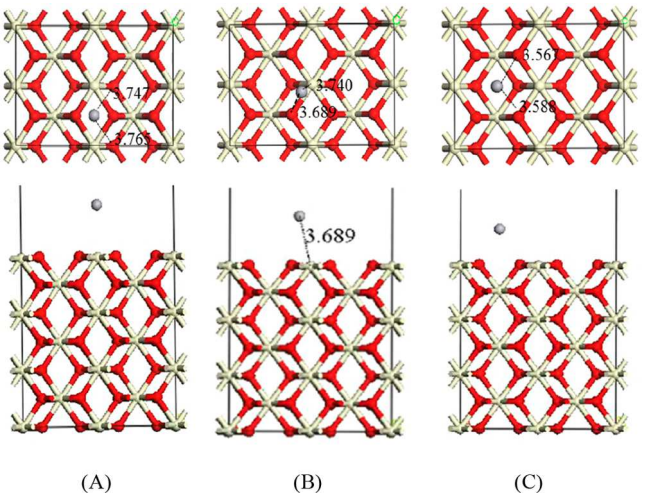

Figure 3. Hg^0 adsorption models on CeO_2(110) surface. (The gray balls stand for Hg.)

Table 1. Adsorption Energies, Geometric Parameters, and Hirshfeld Charges for Hg^0 Adsorption on the CeO_2(110) Surface[a]

configurations	E_{ads} (kJ/mol)	Q_{Hg} (e)	/
3A	−6.36	0.101	3.747/3.765
3B	−6.95	0.121	3.740/3.689
3C	−13.82	0.122	3.567/3.588

[a]X means atoms on the CeO_2 (110) surface.

The Hirshfeld charges of the Hg atom is within the range of 0.101 to 0.122 eV, demonstrating that few electrons are transferred from Hg^0 to the CeO_2(110) substrate. In addition, the partial density of states (PDOS) can reveal the interaction between different atoms. As depicted in Figure 4, the PDOS of Hg and O(6) atoms in the most stable adsorption configuration (model 3C) are used to explain the interaction between Hg^0 and the CeO_2(110) surface. Compared to the preadsorption, the s, p and d-orbitals intensity of the Hg atom decreased after adsorption due to the transfer of the charges

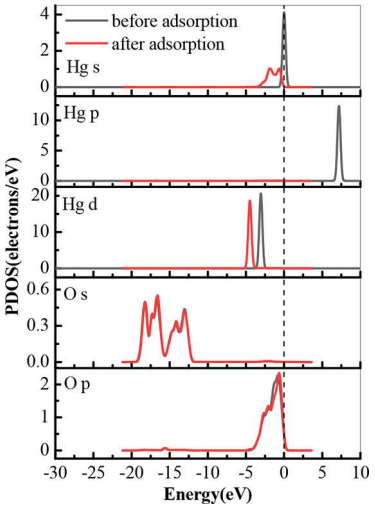

Figure 4. PDOS of Hg and O(6) atoms before and after Hg^0 adsorption in model 3C. The Fermi level (E_f) is set to be zero (dashed line in the figure).

https://dx.doi.org/10.1021/acs.energyfuels.9b04508
Energy Fuels XXXX, XXX, XXX−XXX

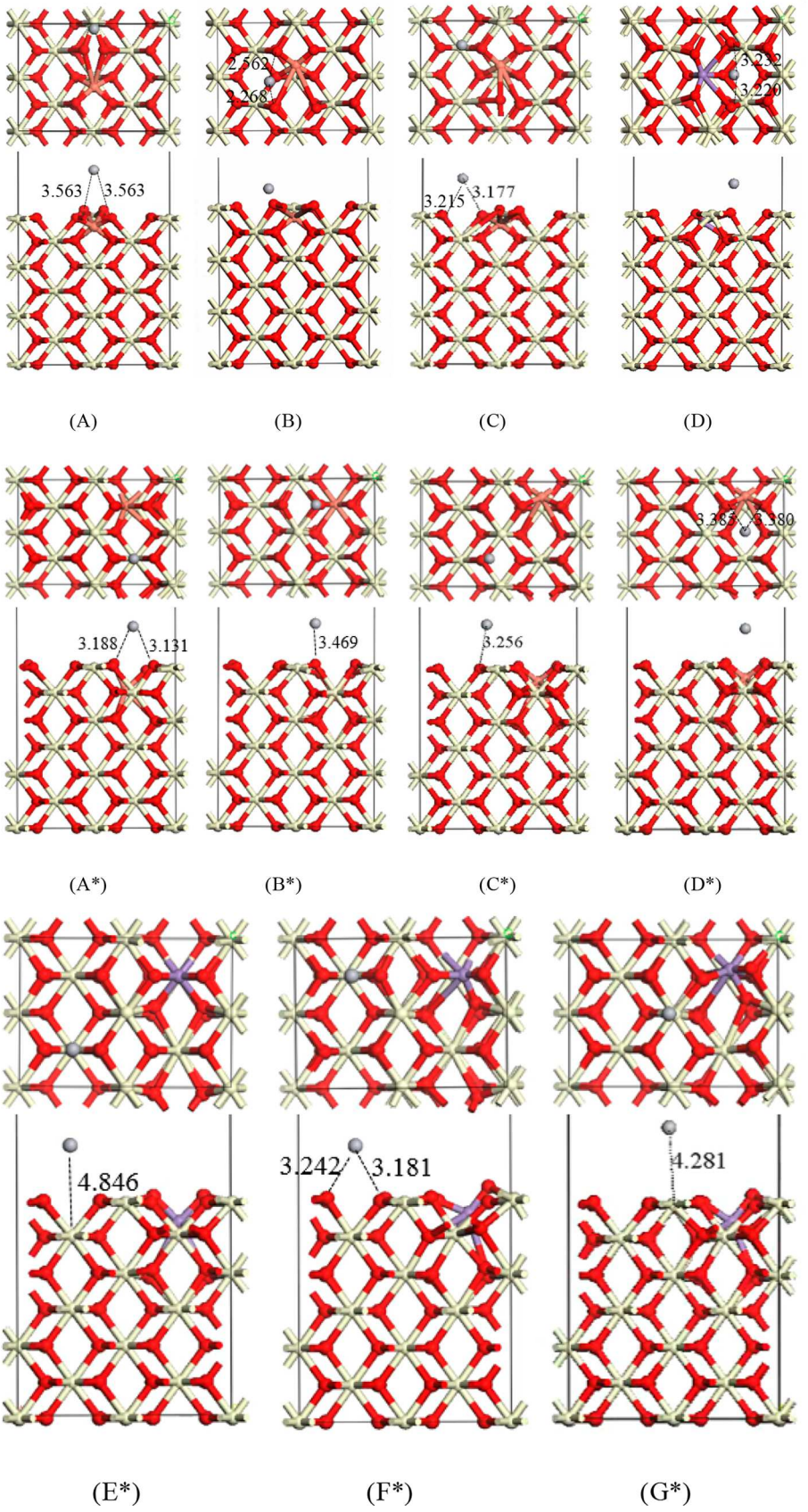

Figure 5. Hg^0 adsorption models on Cu- and Mn-doped $CeO_2(110)$ surfaces (the figure without * meaning Hg^0 adsorbed on Cu/Mn-$CeO_2(110)$ surfaces, the figure with * meaning Hg^0 adsorbed on Cu/Mn-$CeO_2(110)$* surfaces).

https://dx.doi.org/10.1021/acs.energyfuels.9b04508
Energy Fuels XXXX, XXX, XXX−XXX

Table 2. Adsorption Energies and Geometric Parameters for Hg^0 Adsorption on the Cu/Mn-CeO_2(110) and Cu/Mn-CeO_2(110)* Surface[a]

configurations	E_{ads} (kJ/mol)	R(X−Hg) (Å)	configurations	E_{ads} (kJ/mol)	R(X−Hg) (Å)
5A	−182.94	3.563/3.563	5A*	−40.87	3.188/3.131
5B	−186.75	2.562/2.268	5B*	−41.67	3.469
5C	−196.97	3.215/3.177	5C*	−140.23	3.256
5D	−153.98	3.232/3.220	5D*	−146.11	3.385/3.380
			5E*	−56.91	4.846
			5F*	−110.74	3.242/3.181
			5G*	−112.55	4.281

[a]X means atoms on the surfaces.

from Hg to the CeO_2(110) surface, while the s and p-orbitals of the O(6) atom on the CeO_2(110) surface slightly changed, indicating that the CeO_2(110) surface still maintained a stable structure after interacting with Hg^0. Both the Hirshfeld charges and PDOS analysis demonstrated that the interaction between Hg^0 and the CeO_2(110) surface is weak. The experimental results also found that Hg^0 is physically adsorbed on the surface of the CeO_2 catalyst as discussed in experimental section.

3.2. Effect of Cu/Mn Doping on Hg^0 Adsorption. *3.2.1. Effect of Cu/Mn Doping on the Mechanism of Hg^0 Adsorption on the CeO_2(110) Surface.* In order to promote the adsorption performance of Hg^0 on the CeO_2(110) surface, Ce_{suf} and Ce_{sub} atoms were replaced by Cu and Mn atoms to study the effect of heteroatoms on Hg^0 removal. The adsorption configurations and adsorption energies are shown in Figure 5 and Table 2. The results show that the adsorption energies of Hg^0 on Cu-CeO_2(110) and Mn-CeO_2(110) surfaces are −196.97 kJ/mol and −153.98 kJ/mol, much higher than that that on Cu-CeO_2(110)* and Mn-CeO_2(110)* surfaces. Therefore, the Cu-CeO_2(110) and Mn-CeO_2(110) models are used as the substrate due to their higher adsorption energies.

Three stable structures were obtained after the Hg^0 adsorbing on the different sites of the Cu-CeO_2(110) surface, as shown in Figure 5A to C. The adsorption energies ranged from −182.94 kJ/mol to −196.97 kJ/mol, which is much higher than that on the pure CeO_2(110) surface. The most stable adsorption structure is 5C, in which Hg^0 adsorbed on the location of the Ce_{sub} site with the adsorption energy of −196.97 kJ/mol. Meanwhile, the Ce−O bonds closed to the adsorption sites and Cu atom change obviously after Hg^0 adsorption. The distances of Cu−O(2) and Cu−O(3) are 3.308 and 2.697 Å, elongated by 66.23% and 32.3%, respectively. The bond lengths of Cu−O(6) and Cu−O(7) are 1.876 and 1.870 Å, shortened by 8.0% and 8.3% relative to the relevant value of 2.039 Å. Hg^0 eventually tends to the position of O_{sub} no matter where it is placed on the Mn-CeO_2(110) surface, as shown in Figure 5D. The adsorption energy of model 5D is −153.98 kJ/mol. The distances of Mn−O(3) and Mn−O(7) are 3.164 and 3.167 Å, elongated by 55.8% and 54.9%, respectively. The bond lengths of Mn−O(2) and Mn−O(6) are 1.683 and 1.683 Å, shortened by 17.7% and 17.7% relative to the relevant value of 2.044 Å. These results show that the Cu and Mn doping is in favor of Hg^0 adsorption on the CeO_2(110) surface, and the order of Hg^0 adsorption capacity on different surfaces is CeO_2(110) < Mn-CeO_2(110) < Cu-CeO_2(110). One of the reasons for this phenomenon is the lattice distortions caused by Cu and Mn doping strengthening the Hg^0 adsorption.

In order to study the effect of Cu and Mn doping on the Hg^0 adsorption, the PDOS, Valence Band Maximum (VBM), Conduction Band Minimum (CBM), and energy gap of CeO_2(110), Cu-CeO_2(110), and Mn-CeO_2(110) models were calculated, which is shown in Figure 6A and Table 3. The Conduction Band (CB) of three surfaces all showed relatively low values. The CB of the CeO_2(110) model is mainly composed of the Ce 4f orbital, and the Valence Band (VB) of CeO_2(110) model near the Fermi level is composed of O 2p, Ce 3d, and Ce 4f. After Cu doping, the p and d orbitals divide a new small peak at 0.8 eV, causing the CB of Cu-CeO_2(110) to shift to a lower energy than that of the CeO_2(110) model, and the CBM of Cu-CeO_2(110) decreased from −4.561 to −5.142 eV. A new peak occurs at −0.2 eV in the 3d orbitals of Mn-CeO_2(110) model, caused the VB near the Fermi level of Mn-CeO_2(110) shifted to the higher energy level, and the VBM of Mn-CeO_2(110) also increased from −5.983 to −5.470 eV. Figure 6B is the PDOS of Ce, Cu, and Mn atoms on CeO_2(110), Cu-CeO_2(110), and Mn-CeO_2(110) surfaces, which can be used to explain the influence of Cu and Mn doping on surface electronic structures explicitly. Cu 3d presents obvious CB and VB moves over the Fermi level to a higher energy; Mn 3d orbitals have a strong peak at the Fermi level, resulting in the energy gap of Cu-CeO_2(110) and Mn-CeO_2(110) surface decease from 1.422 eV to 0.667 and 0.769 eV. The narrower energy gap could lead to electronic structure change and strengthen the surface reactivity.[39,40] The results from PDOS analysis and the energy gap both agree well with adsorption energy calculation.

3.2.2. Effect of Cu/Mn Doping on Hg^0 Adsorption on the CeO_2(110) by Experimental Method. The contact time between flue gas containing mercury and adsorbent is less than a few seconds. Thus, the first capture efficiency data in Figure 7A are the most representative of the mechanism between mercury and adsorbent. It is noticed that Hg^0 adsorption efficiency at the first 5 min for CeO_2, Mn/CeO_2, and Cu/CeO_2 is 3%, 32%, and 42%, respectively. It is also demonstrated in the bottom right corner of Figure 7A that the Cu and Mn doped CeO_2 have much higher mercury adsorption capacity than CeO_2 adsorbent, and Cu doped CeO_2 has the highest mercury adsorption capacity among the three adsorbents. These results are consistent with the calculated results for the adsorption energy of Hg^0 on the CeO_2(110), Mn-CeO_2(110), and Cu-CeO_2(110) of −13.82, −153.98, and 196.97 kJ/mol, respectively.

The calculated results also were proved through desorption results in Figure 7B. There was only one mercury desorption peak for CeO_2 at 194 °C, which was corresponding to physically adsorbed mercury. While three desorption peaks appeared at Cu/CeO_2, the peak at low temperature was

https://dx.doi.org/10.1021/acs.energyfuels.9b04508
Energy Fuels XXXX, XXX, XXX−XXX

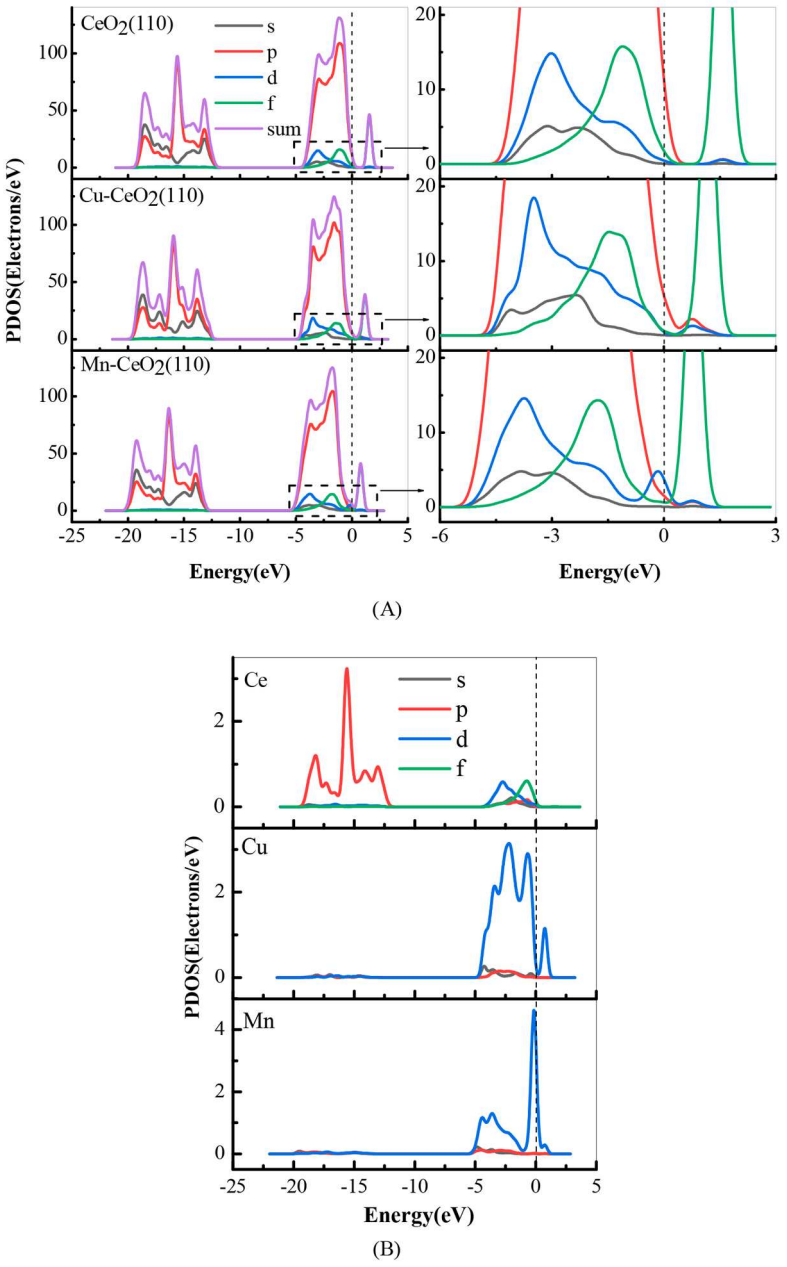

Figure 6. (A) PDOS of $CeO_2(110)$, Cu-$CeO_2(110)$ and Mn-$CeO_2(110)$ surfaces. (B) PDOS of Ce, Cu, and Mn of $CeO_2(110)$, Cu-$CeO_2(110)$, and Mn-$CeO_2(110)$ surfaces. The Fermi level (E_f) is set to be zero (dashed line in the figure).

related to physically adsorbed mercury. The desorption peaks located at 246 and 264 °C were attributed to HgO.[38] The desorption profile of HgO also presented two peaks at 258 and 281 °C on the Mn/CeO_2 catalyst. The results indicated that the doping of Cu and Mn significantly enhanced the Hg^0 adsorption performance; Hg^0 reacted with the oxygen active site to form HgO on the surface of Cu/CeO_2 and Mn/CeO_2, which is consistent with the simulated result.

3.3. Hg^0 and SO_3 Co-Adsorption on the $CeO_2(110)$, Cu-$CeO_2(110)$, and Mn-$CeO_2(110)$ Surfaces. *3.3.1. SO_3 Adsorption on the $CeO_2(110)$, Cu-$CeO_2(110)$, and Mn-$CeO_2(110)$ Surface.* The SO_3 was attached on all possible adsorption sites of the $CeO_2(110)$, Cu-$CeO_2(110)$, and Mn-$CeO_2(110)$ surfaces in the form of verticality and parallelism. After geometric optimization, the stable configurations were obtained, as presented in Figure 8A to E, and the related adsorption energies and geometric parameters are shown in Table 4. SO_3 molecules prefer to bind with the O_{top} site with a parallel configuration on the three surfaces, which is shown in Figure 8A, D, and E. Model 8A shows that SO_3 adsorbed on the $CeO_2(110)$ surface with a adsorption energy of −299.49 kJ/mol, and the S−O bond lengths of SO_3 are 1.460, 1.519, and 1.519 Å, respectively. The distance between the S and

Table 3. Energy Gap of Pure and Cu/Mn Doped $CeO_2(110)$ Surfaces

	VB edge (eV)	CB edge (eV)	energy gap (eV)
1C	−5.983	−4.561	1.422
1D	−5.809	−5.142	0.667
1E	−5.470	−4.701	0.769

https://dx.doi.org/10.1021/acs.energyfuels.9b04508
Energy Fuels XXXX, XXX, XXX−XXX

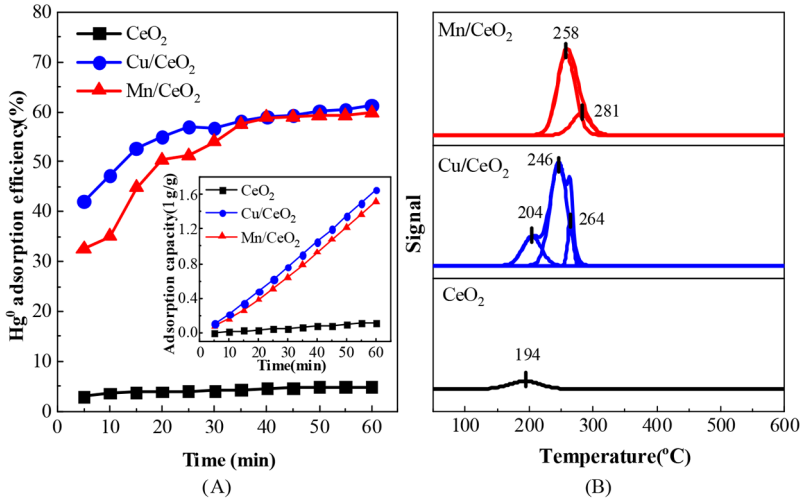

Figure 7. (A) Hg^0 adsorption efficiency of catalysts. (B) Hg^0-TPD patterns of catalysts.

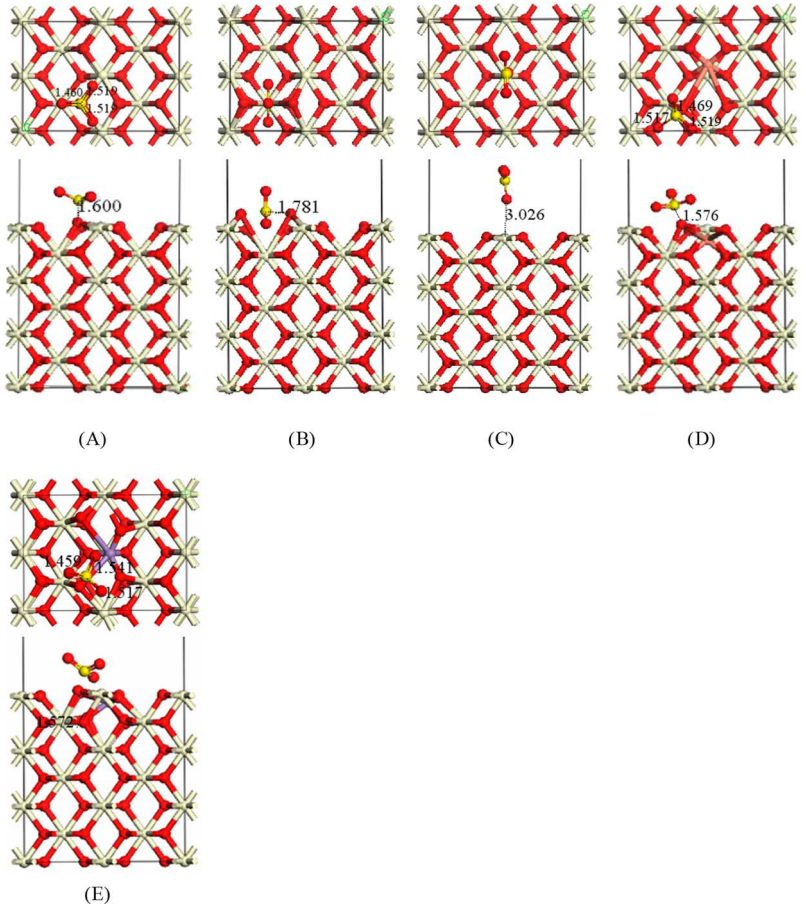

Figure 8. SO_3 adsorption models on $CeO_2(110)$, Cu-$CeO_2(110)$, and Mn-$CeO_2(110)$ surfaces. (The yellow balls stand for S.)

O(6) of $CeO_2(110)$ surface is 1.600 Å, which approaches the calculated bond length (1.46 Å). This phenomenon indicated that adsorbed SO_3 may have reacted with surface O to generate SO_4^{2-} species. The adsorption energies of SO_3 adsorbed on Cu-$CeO_2(110)$ and Mn-$CeO_2(110)$ surfaces are −427.97 and −445.43 kJ/mol, respectively, which is much higher than that on the $CeO_2(110)$ surface, demonstrating that SO_3 is inclined to be adsorbed on Cu and Mn doping surfaces. Meanwhile, the distance between the S and O(6) of Cu-$CeO_2(110)$ and Mn-$CeO_2(110)$ surfaces is 1.576 and 1.572 Å, which is closer than that of the $CeO_2(110)$ surface (1.600), further proving the above results. The adsorption energies of SO_3 adsorbed on $CeO_2(110)$, Cu-$CeO_2(110)$, and Mn-$CeO_2(110)$ surfaces are much higher than that of Hg^0 adsorption on these three surfaces, indicating that SO_3 is more easily adsorbed on the $CeO_2(110)$ surface than Hg^0.

The PDOS analysis of the S and O(6) atoms in model 8A is shown in Figure 9. After adsorption, all orbitals of the S

https://dx.doi.org/10.1021/acs.energyfuels.9b04508
Energy Fuels XXXX, XXX, XXX−XXX

Table 4. Adsorption Energies and Geometric Parameters for All of Models in Figures 8 and 10[a]

configurations	E_{ads} (kJ/mol)	R(X−S/O) (Å)	configurations	E_{ads} (kJ/mol)	R(X−Hg) (Å)
8A	−299.49	1.600	10A	−8.44	3.416
8B	−43.57	1.781	10B	−12.57	3.649/3.542
8C	−11.47	3.026	10C	−13.10	3.679/3.540
8D	−427.97	1.611	10D	−44.38	2.169/2.500
8E	−445.43	1.606	10E	−14.47	3.764/3/547

[a]X means atoms on the surfaces.

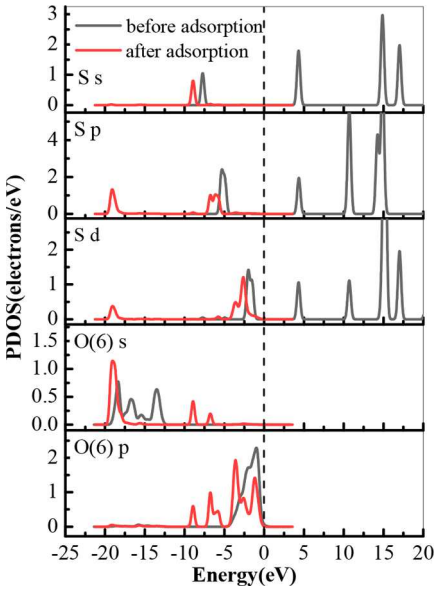

Figure 9. PDOS of S and O(6) atoms before and after SO_3 adsorption in model 8A. The Fermi level (E_f) is set to be zero (dashed line in the figure).

atoms shifted to lower energy states with an obvious decrease of the PDOS value due to a stronger bond caused by greater hybridization. Specifically, a peak at −19.2 eV appeared on the p and d orbitals, which is strongly hybridized with the s orbitals of the O(6) atom. It was also found that the s and p orbitals of the O(6) atom split into several peaks and overlapped with the s, p, and d orbitals of the S atom at −9, −6.5, and −2.7 eV. All of these results confirmed the strong interaction between S and O(6) on the CeO_2(110) surface, further proving that SO_3 reacted with surface O to generate SO_4^{2-} species.

3.3.2. Effect of SO_3 on the Hg^0 Adsorption on CeO_2(110), Cu-CeO_2(110), and Mn-CeO_2(110) Surfaces. SO_3 adsorption on the top of O(6) in model 8A is used as a substrate to study the effect of SO_3 on the Hg^0 adsorption on the CeO_2(110) surface. Hg^0 was placed to on possible adsorption sites on the CeO_2(110) surface in the presence of SO_3. Three stable structures were obtained as shown in Figure 10A, B, and C, and the corresponding adsorption energies are given in Table 4. As shown in model 10C, Hg^0 prefers adsorbing on the location of O_{sub} with the adsorption energy of −13.10 kJ/mol, which is lower than that on the CeO_2(110) surface without SO_3 (−13.82 kJ/mol for model 3C). Hence, SO_3 presented a slightly negative effect on the Hg^0 adsorption on the CeO_2(110) surface.

SO_3 adsorbed on the Cu-CeO_2(110) surface (model 8D) is used as the substrate, and model 10D is the most stable structure. In model 10D, Hg^0 was adsorbed on the location of $hollow_{sub}$ with the adsorption energy of −44.38 kJ/mol. Regarding the Mn-CeO_2(110) surface, SO_3 adsorbed on the top of O(6) in model 8E was used as the substrate. The model 10E is the most stable structure of Hg^0 adsorbed on the Mn-CeO_2(110) surface in the presence of SO_3, with an adsorption energy of −14.47 kJ/mol, respectively. It can be concluded that the adsorption energies of Hg^0 on the Cu and Mn doped CeO_2(110) surface with SO_3 were much lower than that without SO_3 (−196.97 kJ/mol for 5A and −153.98 kJ/mol for 5D). Therefore, SO_3 inhibited the Hg^0 adsorption on the Cu and Mn doped CeO_2(110) surfaces.

In order to further understand the effect of SO_3 on Hg^0 adsorption, the Hirshfeld charges of the surface O atoms (O(1) to O(8)) are calculated, listed in Table 5. If the Hirshfeld charge of one oxygen atom becomes more negative, its propensity for Hg^0 adsorption is enhanced.[30] In Table 5, the 1C, 1D, and 1E are the CeO_2(110), Cu-CeO_2(110), and Mn-CeO_2(110) surfaces, respectively. The 8A, 8D, and 8E correspond to the most stable configuration of SO_3 adsorption on CeO_2(110), Cu-CeO_2(110), and Mn-CeO_2(110) surfaces, respectively. On the basis of the above calculations, the ultimate position of Hg^0 was closest to the surface O atoms, indicating that Hg^0 adsorption on the three surfaces is the consequence of interaction between Hg^0 and surface O atoms. The charges of the surface O atoms on model 8A decreased from −0.359 to −0.346 (O(1)), −0.334 (O(2)), −0.342 (O(3)), −0.349 (O(4)), −0.338 (O(5)), −0.216 (O(6)), −0.345 (O(7)), and −0.354 (O(8)) in the presence of SO_3. The effect of SO_3 on the Hirshfeld charge transfer of Cu-CeO_2(110) and Mn-CeO_2(110) surfaces is similar to that on the CeO_2(110) surface, indicating that SO_3 addition led to the electron transfer among CeO_2(110), Cu-CeO_2(110), and Mn-CeO_2(110) surfaces, particularly reducing the electron accepting ability of surface O atoms; the adsorption capacity of O(1)−O(8) on Hg^0 declined as SO_3 preadsorbed on the surface. Therefore, the existence of SO_3 inhibited the activity of surface oxygen anions in the case of CeO_2.

On the basis of the above analysis, the presence of SO_3 exhibits a negative effect on Hg^0 adsorption mainly due to the following two reasons. First, SO_3 is more easily adsorbed on the CeO_2(110) surface than Hg^0. SO_3 could occupy the active sites prior and competes with Hg^0 when SO_3 and Hg^0 coadsorbed on the three surfaces. Second, SO_3 inhibits the activity of surface oxygen anions in the case of CeO_2, resulting in the negative effect on Hg^0 adsorption. During the experiment, SO_3 was generated by oxidizing SO_2 over a vanadium−titanium catalyst in the presence of O_2;[41] thus, it is difficult to establish an oxygen-free atmosphere to study the effect of SO_3 on Hg^0 without O_2. The effect of SO_3 on Hg^0 in the presence of O_2 will be studied in further theoretical and experimental research.

https://dx.doi.org/10.1021/acs.energyfuels.9b04508
Energy Fuels XXXX, XXX, XXX−XXX

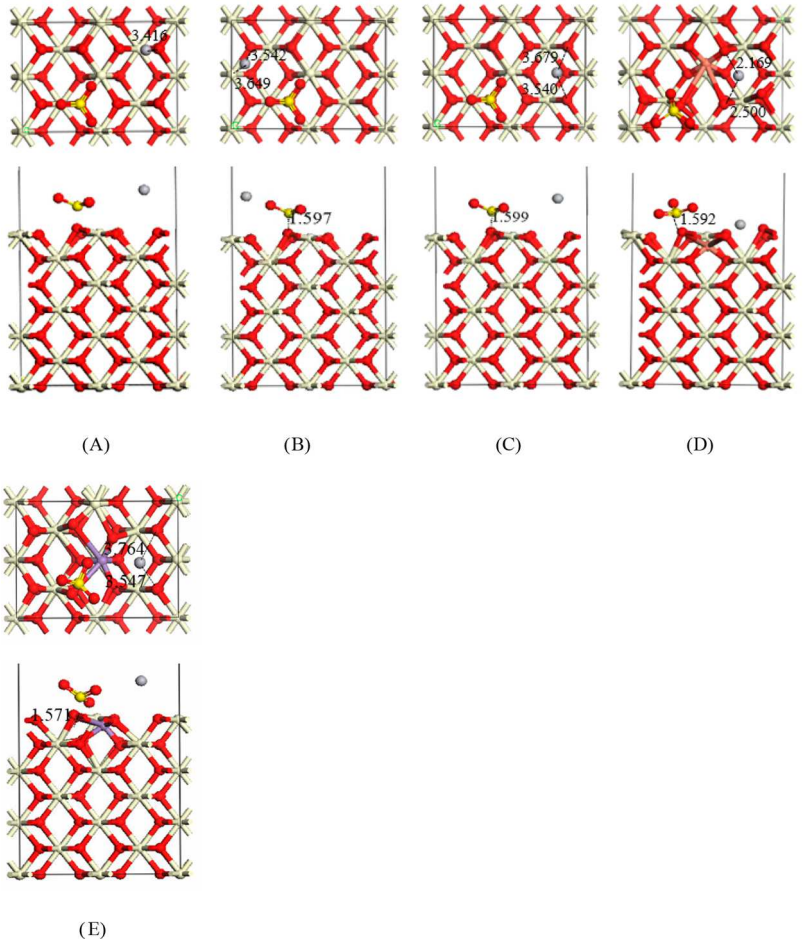

Figure 10. Hg^0 adsorption models on $CeO_2(110)$, Cu-$CeO_2(110)$, and Mn-$CeO_2(110)$ surfaces in the presence of SO_3.

Table 5. Hirshfeld Charges of Surface O Atoms in Different Models

Q_H(e)	1C	8A	1D	8D	1E	8E
O(1)	−0.359	−0.346	−0.360	−0.323	−0.361	−0.342
O(2)	−0.359	−0.334	−0.294	−0.291	−0.302	−0.236
O(3)	−0.359	−0.342	−0.294	−0.307	−0.302	−0.282
O(4)	−0.359	−0.349	−0.360	−0.340	−0.361	−0.349
O(5)	−0.359	−0.338	−0.360	−0.318	−0.361	−0.338
O(6)	−0.359	−0.216	−0.294	−0.220	−0.302	−0.175
O(7)	−0.359	−0.345	−0.294	−0.329	−0.302	−0.328
O(8)	−0.359	−0.354	−0.360	−0.332	−0.361	−0.338

4. CONCLUSIONS

The adsorption process of SO_3 and Hg^0 over pure and Cu/Mn doped $CeO_2(110)$ surfaces was studied by theoretical methods. The calculated results also indicated that the introduction of Cu and Mn strengthened surface relaxation and decreased the energy gap of the $CeO_2(110)$ surface, resulting in improvement of the catalytic activity of the $CeO_2(110)$ surface for Hg^0. The experimental results indicate that the Hg^0 adsorption efficiency is in the order of CeO_2 < Mn/CeO_2 < Cu/CeO_2, which agree well with calculated adsorption energy. There is only the physical desorption peak for CeO_2, while the chemical desorption peak is the main form of mercury adsorption on the Cu/CeO_2 and Mn/CeO_2 catalysts, further demonstrating the chemical adsorption of surface oxygen atoms on Hg^0 in the Cu-$CeO_2(110)$ and Mn-$CeO_2(110)$ surfaces. The simulation results indicate that SO_3 presents a negative effect on Hg^0 adsorption over pure and Cu/Mn doped $CeO_2(110)$ surfaces. The adsorption energy of SO_3 is much higher than Hg^0, and the PDOSs of S and surface O atoms hybridize strongly, causing SO_3 to strongly interact with surface active oxygen to form SO_4^{2-}. Hence, SO_3 competes with Hg^0 for surface active oxygen sites. Meanwhile, SO_3 preadsorbed on the $CeO_2(110)$ surface decreases the activity of surface O atoms (O(1) to O(8)), directly causing a negative effect on Hg^0 adsorption.

AUTHOR INFORMATION

Corresponding Authors

Tao Wang − *Key Laboratory of Condition Monitoring and Control for Power Plant Equipment, Ministry of Education, North China Electric Power University, Beijing 102206,*

https://dx.doi.org/10.1021/acs.energyfuels.9b04508
Energy Fuels XXXX, XXX, XXX−XXX

China; orcid.org/0000-0003-1293-3185;
Email: wangtao0420@163.com

Yongsheng Zhang − *Key Laboratory of Condition Monitoring and Control for Power Plant Equipment, Ministry of Education, North China Electric Power University, Beijing 102206, China;* orcid.org/0000-0002-1104-5605;
Email: yszhang@ncepu.edu.cn

Authors

Yihuan Yang − *Key Laboratory of Condition Monitoring and Control for Power Plant Equipment, Ministry of Education, North China Electric Power University, Beijing 102206, China*

Jiawei Wang − *Key Laboratory of Condition Monitoring and Control for Power Plant Equipment, Ministry of Education, North China Electric Power University, Beijing 102206, China*

Baharak Sajjadi − *Department of Chemical Engineering, University of Mississippi, Oxford, Mississippi 38677-1848, United States;* orcid.org/0000-0001-6609-0705

Wei-Yin Chen − *Department of Chemical Engineering, University of Mississippi, Oxford, Mississippi 38677-1848, United States*

Wei-Ping Pan − *Key Laboratory of Condition Monitoring and Control for Power Plant Equipment, Ministry of Education, North China Electric Power University, Beijing 102206, China*

Complete contact information is available at:
https://pubs.acs.org/10.1021/acs.energyfuels.9b04508

Notes

The authors declare no competing financial interest.

■ ACKNOWLEDGMENTS

This work was supported by National Natural Science Foundation of China (51706069), Wei-Yin Chen's work is supported by the National Science Foundation of America (1632899).

■ REFERENCES

(1) Tao, S.; Li, C.; Fan, X.; Zeng, G.; Lu, P.; Zhang, X.; Wen, Q.; Zhao, W.; Luo, D.; Fan, C. Activated coke impregnated with cerium chloride used for elemental mercury removal from simulated flue gas. *Chem. Eng. J.* **2012**, *210*, 547−556.

(2) Fan, X.; Li, C.; Zeng, G.; Zhang, X.; Tao, S.; Lu, P.; Tan, Y.; Luo, D. Hg^0 Removal from Simulated Flue Gas over CeO_2/HZSM-5. *Energy Fuels* **2012**, *26* (4), 2082−2089.

(3) Presto, A. A.; Granite, E. J. Survey of Catalysts for Oxidation of Mercury in Flue Gas. *Environ. Sci. Technol.* **2006**, *40* (18), 5601−5609.

(4) Li, H.; Wu, C.-Y.; Li, Y.; Zhang, J. Superior activity of MnOx-CeO_2/TiO_2 catalyst for catalytic oxidation of elemental mercury at low flue gas temperatures. *Appl. Catal., B* **2012**, *111*−*112*, 381−388.

(5) Wang, Z.; Liu, J.; Zhang, B.; Yang, Y.; Zhang, Z.; Miao, S. Mechanism of Heterogeneous Mercury Oxidation by HBr over V_2O_5/TiO_2 Catalyst. *Environ. Sci. Technol.* **2016**, *50* (10), 5398−5404.

(6) Guo, P.; Guo, X.; Zheng, C. Roles of γ-Fe_2O_3 in fly ash for mercury removal: Results of density functional theory study. *Appl. Surf. Sci.* **2010**, *256* (23), 6991−6996.

(7) Liu, J.; He, M.; Zheng, C.; Chang, M. Density functional theory study of mercury adsorption on V_2O_5(001) surface with implications for oxidation. *Proc. Combust. Inst.* **2011**, *33* (2), 2771−2777.

(8) Wang, T.; Wan, Z.; Yang, X.; Zhang, X.; Niu, X.; Sun, B. Promotional effect of iron modification on the catalytic properties of Mn-Fe/ZSM-5 catalysts in the Fast SCR reaction. *Fuel Process. Technol.* **2018**, *169*, 112−121.

(9) Wang, T.; Liu, H.; Zhang, X.; Liu, J.; Zhang, Y.; Guo, Y.; Sun, B. Catalytic conversion of NO assisted by plasma over Mn-Ce/ZSM5-multi-walled carbon nanotubes composites: Investigation of acidity, activity and stability of catalyst in the synergic system. *Appl. Surf. Sci.* **2018**, *457*, 187−199.

(10) Liu, J.; Du, Y.; Liu, J.; Zhao, Z.; Cheng, K.; Chen, Y.; Wei, Y.; Song, W.; Zhang, X. Design of MoFe/Beta@CeO_2 catalysts with a core-shell structure and their catalytic performances for the selective catalytic reduction of NO with NH_3. *Appl. Catal., B* **2017**, *203*, 704−714.

(11) Liu, J.; Liu, J.; Zhao, Z.; Wei, Y.; Song, W. Fe-Beta@CeO_2 Core-Shell Catalyst with Tunable Shell Thickness for Selective Catalytic Reduction of NOx with NH_3. *AIChE J.* **2017**, *63* (10), 4430−4441.

(12) Liu, J.; Zhao, Z.; Xu, C.; Liu, J. Structure, synthesis, and catalytic properties of nanosize cerium-zirconium-based solid solutions in environmental catalysis. *Chin. J. Catal.* **2019**, *40* (10), 1438−1487.

(13) Liu, J.; Cheng, H.; Bao, J.; Zhang, P.; Liu, M.; Leng, Y.; Zhang, Z.; Tao, R.; Liu, J.; Zhao, Z.; Dai, S. Aluminum hydroxide-mediated synthesis of mesoporous metal oxides by a mechanochemical nanocasting strategy. *J. Mater. Chem. A* **2019**, *7*, 22977−22985.

(14) Spezzati, G.; Benavidez, A. D.; DeLaRiva, A. T.; Su, Y.; Hofmann, J. P.; Asahina, S.; Olivier, E. J.; Neethling, J. H.; Miller, J. T.; Datye, A. K.; Hensen, E. J. M. CO oxidation by Pd supported on CeO_2(100) and CeO_2(111) facets. *Appl. Catal., B* **2019**, *243*, 36−46.

(15) Tang, Y.; Zhang, H.; Cui, L.; Ouyang, C.; Shi, S.; Tang, W.; Li, H.; Lee, J.-S.; Chen, L. First-principles investigation on redox properties of M-doped CeO_2 (M = Mn, Pr, Sn, Zr). *Phys. Rev. B: Condens. Matter Mater. Phys.* **2010**, *82* (12), 125104.

(16) Wang, H.-F.; Gong, X.-Q.; Guo, Y.-L.; Guo, Y.; Lu, G. Z.; Hu, P. A Model to Understand the Oxygen Vacancy Formation in Zr-Doped CeO_2: Electrostatic Interaction and Structural Relaxation. *J. Phys. Chem. C* **2009**, *113* (23), 10229−10232.

(17) Lu, Y.-H.; Chen, H.-T. Computational Investigation of NO_2 Adsorption and Reduction on Ceria and M-Doped CeO_2(111) (M = Mn, Fe) Surfaces. *J. Phys. Chem. C* **2014**, *118* (19), 10043−10052.

(18) Cui, L.; Tang, Y.; Zhang, H.; Hector, L.; Ouyang, C.; Shi, S.; Li, H.; Chen, L. First-principles investigation of transition metal atom M (M = Cu, Ag, Au) adsorption on CeO_2(110). *Phys. Chem. Chem. Phys.* **2012**, *14*, 1923−33.

(19) Wang, J.; Gong, X.-Q. A DFT+U study of V, Cr and Mn doped CeO_2(111). *Appl. Surf. Sci.* **2018**, *428*, 377−384.

(20) Guo, C.; Wei, S.; Zhou, S.; Zhang, T.; Wang, Z.; Ng, S.-P.; Lu, X.; Wu, C.-M. L.; Guo, W. Initial Reduction of CO_2 on Pd-, Ru-, and Cu-Doped CeO_2(111) Surfaces: Effects of Surface Modification on Catalytic Activity and Selectivity. *ACS Appl. Mater. Interfaces* **2017**, *9* (31), 26107−26117.

(21) Song, Y.-L.; Yin, L.-L.; Zhang, J.; Hu, P.; Gong, X.-Q.; Lu, G. A DFT + U study of CO oxidation at CeO_2(110) and (111) surfaces with oxygen vacancies. *Surf. Sci.* **2013**, *618*, 140−147.

(22) Baudin, M.; Wójcik, M.; Hermansson, K. Dynamics, Structure and Energetics of the (111), (011) and (001) Surfaces of Ceria. *Surf. Sci.* **2000**, *468*, 51−61.

(23) Zhao, L.; Wu, Y.; Han, J.; Lu, Q.; Yang, Y.; Zhang, L. Mechanism of Mercury Adsorption and Oxidation by Oxygen over the CeO_2 (111) Surface: A DFT Study. *Materials* **2018**, *11*, 485.

(24) Li, H.; Liu, S.; Yang, J.; Liu, Y.; Hu, Y.; Feng, S.; Yang, Z.; Zhao, J.; Qu, W. Role of SO_2 and H_2O in the mercury adsorption on ceria surface: A DFT study. *Fuel* **2020**, *260*, 116289.

(25) Zhang, J.; Gong, X.-Q.; Lu, G. Catalytic activities of CeO_2(110)-2 × 1 reconstructed surface. *Surf. Sci.* **2015**, *632*, 164−173.

(26) Yang, Y.; Liu, J.; Zhang, B.; Zhao, Y.; Chen, X.; Shen, F. Experimental and theoretical studies of mercury oxidation over CeO_2-WO_3/TiO_2 catalysts in coal-fired flue gas. *Chem. Eng. J.* **2017**, *317*, 758−765.

https://dx.doi.org/10.1021/acs.energyfuels.9b04508
Energy Fuels XXXX, XXX, XXX−XXX

(27) Zhuang, Y.; Laumb, J.; Liggett, R.; Holmes, M.; Pavlish, J. Impacts of acid gases on mercury oxidation across SCR catalyst. *Fuel Process. Technol.* **2007**, *88* (10), 929−934.
(28) Sjostrom, S.; Dillon, M.; Donnelly, B.; Bustard, J.; Filippelli, G.; Glesmann, R.; Orscheln, T.; Wahlert, S.; Chang, R.; O'Palko, A. Influence of SO_3 on mercury removal with activated carbon: Full-scale results. *Fuel Process. Technol.* **2009**, *90* (11), 1419−1423.
(29) Cao, Y.; Chen, B.; Wu, J.; Cui, H.; Smith, J.; Chen, C.-K.; Chu, P.; Pan, W.-P. Study of Mercury Oxidation by a Selective Catalytic Reduction Catalyst in a Pilot-Scale Slipstream Reactor at a Utility Boiler Burning Bituminous Coal. *Energy Fuels* **2007**, *21* (1), 145−156.
(30) He, P.; Wu, J.; Jiang, X.; Pan, W.; Ren, J. Effect of SO_3 on elemental mercury adsorption on a carbonaceous surface. *Appl. Surf. Sci.* **2012**, *258* (22), 8853−8860.
(31) Ji, W.; Shen, Z.; Tang, Q.; Yang, B.; Fan, M. A DFT study of Hg^0 adsorption on $Co_3O_4(110)$ surface. *Chem. Eng. J.* **2016**, *289*, 349−355.
(32) Delley, B. From molecules to solids with the DMol3 approach. *J. Chem. Phys.* **2000**, *113* (18), 7756−7764.
(33) Perdew, J. P.; Burke, K.; Ernzerhof, M. Generalized Gradient Approximation Made Simple. *Phys. Rev. Lett.* **1996**, *77* (18), 3865−3868.
(34) Perdew, J. P.; Burke, K.; Wang, Y. Generalized gradient approximation for the exchange-correlation hole of a many-electron system. *Phys. Rev. B: Condens. Matter Mater. Phys.* **1996**, *54* (23), 16533−16539.
(35) Gerward, L.; Staun Olsen, J.; Petit, L.; Vaitheeswaran, G.; Kanchana, V.; Svane, A. Bulk modulus of CeO_2 and PrO_2-An experimental and theoretical study. *J. Alloys Compd.* **2005**, *400* (1), 56−61.
(36) Kumari, N.; Haider, A.; Agarwal, M.; Sinha, N.; Basu, S. Role of Reduced $CeO_2(110)$ Surface for CO_2 Reduction to CO and Methanol. *J. Phys. Chem. C* **2016**, *120* (30), 16626−16635.
(37) Rad, A. S.; Shabestari, S. S.; Mohseni, S.; Aghouzi, S. A. Study on the adsorption properties of O_3, SO_2, and SO_3 on B-doped graphene using DFT calculations. *J. Solid State Chem.* **2016**, *237*, 204−210.
(38) Wang, T.; Liu, J.; Yang, Y.; Sui, Z.; Zhang, Y.; Wang, J.; Pan, W.-P. Catalytic conversion of mercury over Ce doped Mn/SAPO-34 catalyst: Sulphur tolerance and SO_2/SO_3 conversion. *J. Hazard. Mater.* **2020**, *381*, 120986.
(39) Wu, Y.-w.; Ali, Z.; Lu, Q.; Liu, J.; Xu, M.-x.; Zhao, L.; Yang, Y.-p. Effect of WO_3 doping on the mechanism of mercury oxidation by HCl over $V_2O_5/TiO_2(001)$ surface: Periodic density functional theory study. *Appl. Surf. Sci.* **2019**, *487*, 369−378.
(40) Calatayud, M.; Mguig, B.; Minot, C. A DFT study on the hydrated V_2O_5-TiO_2-anatase catalyst: stability of monomeric species. *Theor. Chem. Acc.* **2005**, *114* (1), 29−37.
(41) Yang, Z.; Li, H.; Qu, W.; Zhang, M.; Feng, Y.; Zhao, J.; Yang, J.; Shih, K. Role of Sulfur Trioxide (SO_3) in Gas-Phase Elemental Mercury Immobilization by Mineral Sulfide. *Environ. Sci. Technol.* **2019**, *53* (6), 3250−3257.

https://dx.doi.org/10.1021/acs.energyfuels.9b04508
Energy Fuels XXXX, XXX, XXX−XXX